THE JOURNAL OF PHYSICAL CHEMISTRY C

pubs.acs.org/JPCC

Article

Favoring the Growth of High-Quality, Three-Dimensional Supercrystals of Nanocrystals

Emanuele Marino, Austin W. Keller, Di An, Sjoerd van Dongen, Thomas E. Kodger, Katherine E. MacArthur, Marc Heggen, Cherie R. Kagan, Christopher B. Murray, and Peter Schall*

Cite This: *J. Phys. Chem. C* 2020, 124, 11256–11264

Read Online

ACCESS | Metrics & More | Article Recommendations | Supporting Information

ABSTRACT: A recently developed emulsion-templated assembly method promises the scalable, low-cost, and reproducible fabrication of hierarchical nanocrystal (NC) superstructures. These superstructures derive properties from the unique combination of choices of NC building blocks and superstructure morphology and therefore realize the concept of "artificial solids". To control the final properties of these superstructures, it is essential to control the assembly conditions that yield distinct architectural morphologies. Here, we explore the phase-space of experimental parameters describing the emulsion-templated assembly including temperature, interfacial tension, and NC polydispersity and demonstrate which conditions lead to the growth of the most crystalline NC superstructures or supercrystals. By using a combination of electron microscopy and small-angle X-ray scattering, we show that slower assembly kinetics, softer interfaces, and lower NC polydispersity contribute to the formation of supercrystals with grain sizes up to 600 nm, while reversing these trends yields glassy solids. These results provide a clear path to the realization of higher-quality supercrystals, necessary to many applications.

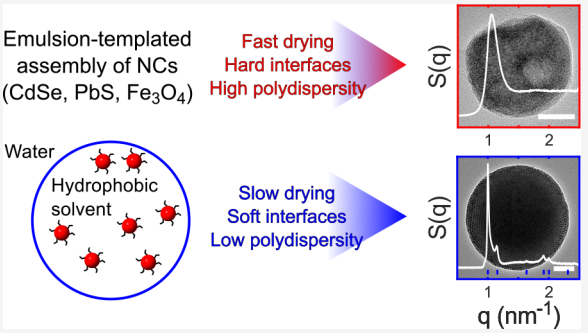

INTRODUCTION

The desire for increased miniaturization and greater flexibility in heterointegration of optical and electronic components demands the introduction of a new class of nanoscale building blocks. Crystalline nanoparticles, or nanocrystals (NCs), are an ideal choice as they can be prepared through inexpensive chemical processes in a wide range of compositions, sizes, and shapes. However, to be harnessed in devices, NCs must first be assembled into robust and reproducible superstructures.[1] This assembly process is the result of the superposition of several concurrent colloidal interactions allowing NCs to condense into a solid.[2] Importantly, the resulting properties of these NC solids are a combination of those of the constituent building blocks and of the structural morphology of the solid. For instance, glassy solids based on semiconductor NCs feature inefficient charge transport through percolation,[3] while crystalline solids allow for more efficient transport through the emergence of collective electronic states.[4−8] Consequently, high-quality NC-based crystals, or supercrystals, are required to drive the advancement toward novel physical phenomena and improved device performance.

Recently, an emulsion-templated approach has emerged as a way to produce high-quality supercrystals.[9−13] This method relies on the preparation of an oil-in-water emulsion where the dispersed phase is composed of a dilute dispersion of NCs in a volatile hydrophobic solvent, while the continuous phase is an aqueous solution of surfactant that stabilizes the liquid/liquid interface (Figure 1). As the dispersed phase slowly dissolves into the continuous phase and evaporates,[14] the droplets decrease in size and the NC volume fraction within the droplets, ϕ, increases. Eventually, when a critical volume fraction ϕ_c is reached, crystals can nucleate and grow: if the NC volume fraction increases slowly enough, the NCs can rearrange to reach their minimum energy configuration thereby leading to the growth of large supercrystals.[15] Since the rate of increase in volume fraction depends on the evaporation rate, which can be tuned by the solubility of the dispersed phase in the continuous phase, this emulsion-templated platform is ideally suited to produce high-quality NC-based supercrystals and study their growth dynamics in real time. This was recently demonstrated by two *in situ* studies that followed the kinetics of supercrystal formation by measuring the small-angle X-ray scattering (SAXS) patterns of the evaporating emulsion as a function of time.[16,17] These results highlighted the contribution of ligands bound to the NC surface in driving supercrystal nucleation and growth, a departure from classical hard sphere behavior. For example, hard sphere crystals are expected to

Received: March 30, 2020
Revised: April 27, 2020
Published: April 28, 2020

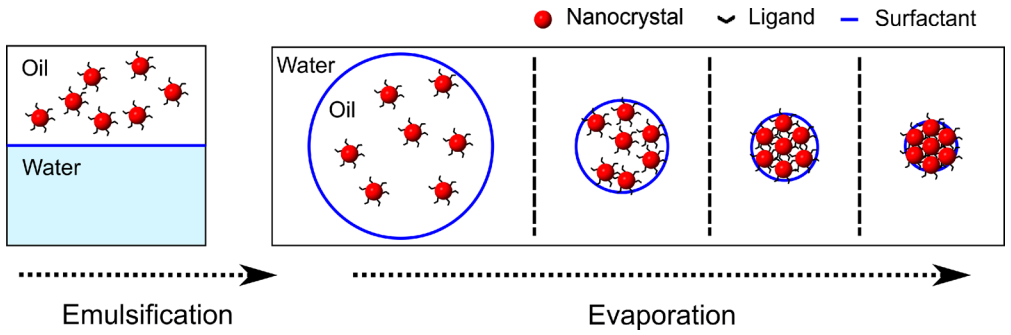

Figure 1. Schematic of the emulsion-templated assembly process. A dispersion of NCs in a hydrophobic volatile solvent is layered on an aqueous solution of surfactant. The emulsification of this two-phase system leads to droplets containing the NC dispersion. As the hydrophobic phase, also known as the dispersed phase, slowly dissolves into the aqueous phase, or continuous phase, the NC volume fraction increases, eventually leading to supercrystal nucleation.

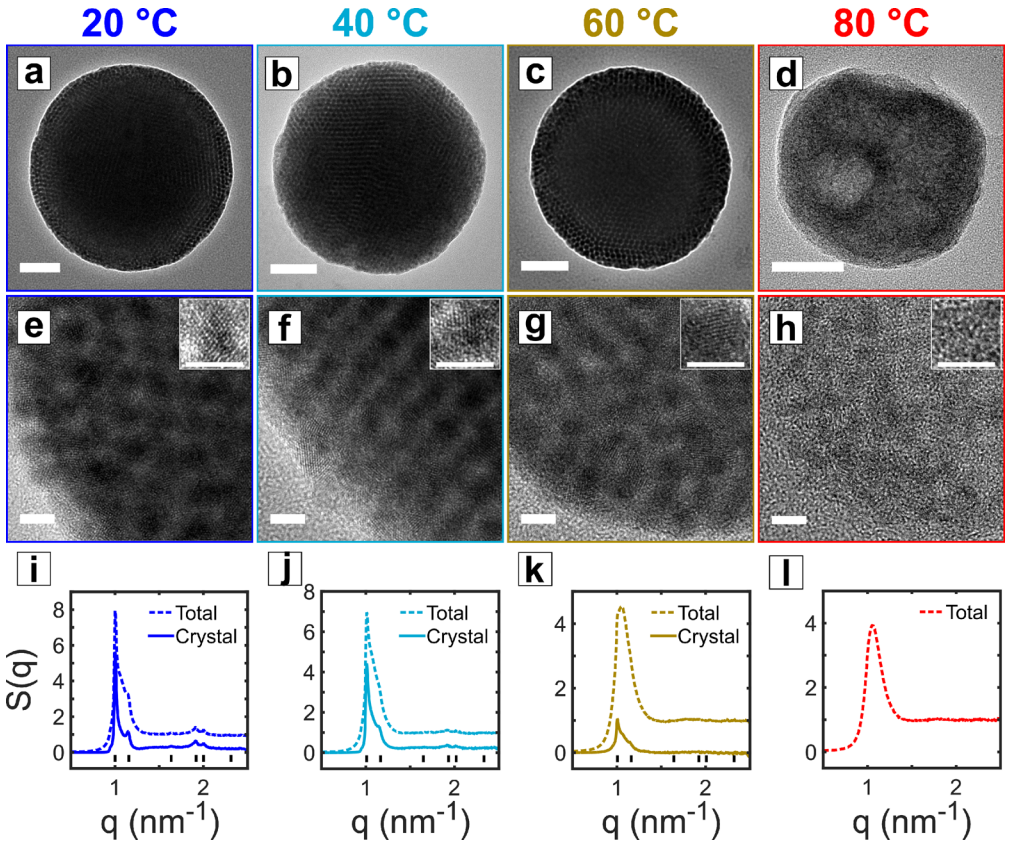

Figure 2. Influence of the evaporation rate on supercrystal quality. Intermediate (a–d) and high (e–h) resolution TEM micrographs of superstructures assembled from an emulsion dried at the indicated temperatures. The dispersed phase consisted of a dispersion of $\sigma = 5.6 \pm 0.7$ nm CdSe NCs in cyclohexane at an initial volume fraction of $\phi \approx 0.09\%$, while the continuous phase consisted of a solution of 6 g/L SDS in water. The insets show a zoomed-in view of a NC embedded in the superstructure. Scale bars: 50 nm (a–d) and 5 nm (e–h). (i–l) Experimental structure factors of supercrystals dried at the indicated temperatures.

nucleate at volume fractions of $\phi_c \approx 49\%$,[15] while these *in situ* studies showed that NC-based supercrystals nucleate at significantly lower volume fractions of $\phi_c \approx 15–20\%$ due to the presence of the ligand shell.[16,17] In addition, the presence of multiple attractive and repulsive interactions between NCs demand the introduction of a reliable model to predict the crystallization behavior of these nanoscale building blocks.[16,18]

In this paper, we experimentally investigate the effect of evaporation rate, surface tension, and type of dispersing solvent on the growth of high-quality NC supercrystals. We use a combination of SAXS and electron microscopy (TEM and SEM) to determine the crystallinity and crystal size in superstructures grown from cadmium selenide (CdSe) NCs. Doing so, we are able to delineate regions of the phase space that support the formation of supercrystals. Within these regions, we find the conditions that lead to the largest and highest-quality supercrystals. Furthermore, we identify a tolerance window on the polydispersity (PD) of the NC building blocks that still leads to crystallization.[19] Finally, we demonstrate the wider applicability of the emulsion-templated assembly by applying it to superstructures consisting of lead sulfide (PbS) and iron oxide (Fe_3O_4) NCs, the formation of which we follow *in situ*. These results provide an important and

https://dx.doi.org/10.1021/acs.jpcc.0c02805
J. Phys. Chem. C 2020, 124, 11256–11264

necessary insight that should serve as a basis to produce high-quality supercrystals.

EXPERIMENTAL DETAILS

We synthesize oleate-functionalized CdSe, PbS, and Fe_3O_4 NCs by following procedures reported in the literature.[20−22] A detailed description of these procedures and electron micrographs of the dispersed NCs are available in the Supporting Information (Figures S1−S3). After washing, we redisperse the NCs in the desired hydrophobic solvent. The NC concentration is determined by using sizing curves reported in the literature for CdSe and PbS[21,23] and by measuring the dry mass for Fe_3O_4. The continuous phase of the emulsion consists of a solution of sodium dodecyl sulfate (SDS) in Milli-Q water at a concentration of 6 mg/mL, unless otherwise stated. To prepare the emulsions, we add 8 mL of the aqueous surfactant solution to a 20 mL scintillation vial. Subsequently, we add 2 mL of a 5 mg/mL NC dispersion. After capping the vial, we thoroughly mix its contents using a vortex mixer for 30 s. The vial is then uncapped and, after the addition of a 1 in. stir bar, placed in a glycerol bath stabilized at the desired temperature (20−80°C). The emulsion is left to dry in the fumehood while being stirred at 400 rpm. After drying for 12 h (overnight), we wash the resulting supercrystals twice by centrifuging at 3000*g* for 1 h, followed by redispersion in 6 mg/mL SDS in water to reach a supercrystal concentration of 5 mg/mL. For TEM measurements, we remove the unbound surfactant by washing twice in deionized water. We then drop-cast 10 μL of the supercrystal dispersion on a carbon-coated copper grid and dry the grid overnight at room temperature under vacuum (less than 0.1 Torr). Small-angle X-ray scattering (SAXS) patterns are recorded from a 2mm quartz capillary tube filled with a supercrystal dispersion at a concentration of 5 mg/mL in 6 mg/mL SDS in water. *In situ* drying experiments are performed by preparing the emulsion as described above but using a surfactant concentration of 24 mg/mL and using a peristaltic pump to flow the emulsion through a custom-made flow-cell.

RESULTS AND DISCUSSION

Evaporation Rate. We investigate the influence of the evaporation rate on the final crystallinity of the superstructures for σ = 5.6 ± 0.7 nm CdSe NCs in cyclohexane. After the droplets were completely dried and washed, we observed that the superstructures retained their spherical morphology as seen in the TEM micrographs shown in Figure 2 and S6. A closer look at the superstructures dried at 20 °C reveals their crystallinity (Figure 2a,e). However, superstructures of comparable sizes dried at higher temperatures (40−80 °C) show a gradual transition from crystalline to amorphous (Figure 2b−d,f−h). We attribute this transition from crystalline to amorphous superstructures to the decreased drying time of the droplets at higher temperatures, from ≈10 h at 20 °C to ≈0.5 h at 80 °C, not allowing the superstructures to reach their thermodynamically stable configuration. This process is analogous to the formation of an atomic solid, where quench rates faster than the crystallization time induce the formation of a glass.[24] To minimize the possibility of day-to-day variations and aging of the NC dispersion, these samples were prepared simultaneously and from the same NC batch.

By focusing on the thinner edge of the superstructures, Figure 2e−h, we can distinguish both the NC planes of the superstructure as well as the atomic planes of the individual NCs; see insets in Figure 2e−h. The atomic planes do not show any sign of coherent orientation throughout the superstructure as expected for well-passivated NC systems where oriented attachment is not expected to occur; see Figure 2e.[25] Higher drying temperatures affect the colloidal order of the superstructures. While the superstructures dried at 60 °C still display supercrystalline order, this is no longer the case for the superstructures dried at 80 °C, as clearly seen in the TEM micrograph and in an image distortion of the atomic lattice planes. This is further confirmed by the fast-Fourier transforms of the TEM micrographs, as shown in Figures S4 and S5.

To further analyze the effect of evaporation rate on the long-range order of the superstructures, we use SAXS to characterize the colloidal crystalline superstructures. After background subtraction, we derive the structure factor $S(q)$ by dividing the scattering pattern $I(q)$ of a dispersion of superstructures by the form factor $P(q)$ of a dilute dispersion of NCs: The results are shown in Figure 2i−l (dashed lines). The structure factor extracted from the superstructures dried at 20 °C consists of a collection of sharp reflections, where the position q_i of the i-th reflection reproduces well the sequence

$$q_i/q_1 = 1, \sqrt{4/3}, \sqrt{8/3}, \sqrt{11/3}, \sqrt{12/3}$$

identifying the face-centered cubic (FCC) structure (solid ticks). Furthermore, the flat background at higher q reveals the presence of a residual amorphous component. As the drying temperature increases, the reflection peaks gradually lose definition to eventually result in a single, broad peak for the sample dried at 80 °C. This type of structure factor describes a solid with no long-range order, a colloidal glass.[26] If we assume the shape of the glassy structure factor to be temperature-independent, we can take advantage of it to decouple the contributions to the total structure factor of ordered and disordered domains.[27] By subtracting the glassy contribution from the total structure factor, we recover the characteristic structure factor of a crystalline solid (solid lines, see the Supporting Information for more details). To quantify the fraction of NCs forming supercrystals, we define the crystallinity as[28]

$$X = \int_{q_1} S_{Crystal}(q)dq / \int_{q_1} S_{Total}(q)dq$$

where the integration is performed over the first reflection peak. Here, we assume that the crystalline and amorphous assemblies have the same intensity per assembly unit, which seems reasonable given their similar density and same size distribution. We also calculate the volume fraction ϕ of the FCC crystalline component from

$$\phi = 100\% \times (\sigma q_1)^3/(36\sqrt{3}\pi^2)$$

as well as the average crystalline grain size

$$\xi = 2\pi K/\Delta q_1$$

where K = 1.0747 is the Scherrer constant for a spherical crystal and Δq_1 is the full-width at half-maximum of the first reflection.[29] The results summarized in Table 1 illustrate the transition from crystalline to amorphous superstructures as a result of the increasing evaporation rate. The samples dried at 20 and 40 °C feature similar crystallinity values of $X \approx 67\%$ and 58%, quickly dropping to 22% at 60 °C. This sudden drop in crystallinity is accompanied by a gradual decrease in the average crystal size from $\xi \approx 270$ to 200 nm. In contrast, the

https://dx.doi.org/10.1021/acs.jpcc.0c02805
J. Phys. Chem. C 2020, 124, 11256−11264

Table 1. Influence of Evaporation Rate on the Quality of Supercrystals Based on σ = 5.6 ± 0.7 nm CdSe NCs[a]

Temperature, T	Crystallinity, X	Volume fraction, ϕ	Crystal size, ξ
°C	%	%	nm
20	67.1 ± 0.1	28.4 ± 0.2	266.2 ± 0.5
40	58.1 ± 0.1	29.2 ± 0.2	224.4 ± 0.4
60	21.60 ± 0.04	28.8 ± 0.2	197.6 ± 0.4
80	0		

[a]Dispersed phase: cyclohexane; continuous phase: 6 g/L SDS in water.

volume fraction of the crystalline component remains unaffected by the evaporation rate, amounting to $\phi \approx 29\%$. This is consistent with previous reports showing that the inorganic volume fraction of FCC supercrystals based on CdSe saturates at around 30% after supercrystal densification.[16]

Interfacial Tension and Choice of Solvent. In addition to evaporation rate, interfacial tension may play a role in the emulsion-templating of supercrystals. While maintaining a constant temperature, we decrease the interfacial tension by increasing the surfactant concentration in the continuous phase from 6 to 60 mg/mL. Doing so results in remarkably sharper reflections and therefore in significantly higher crystallinity, from $X \approx 61\%$ to 80%, and average crystalline grain size from $\xi \approx 241$ nm to 497 nm, while leaving the type of crystalline structure and volume fraction unaltered (Figure 3a). The interfacial tension represents the energetic cost of the interface per unit area; therefore, a decrease in the interfacial tension will result in a more deformable liquid/liquid interface. We speculate that this more flexible interface more efficiently accommodates the growing crystallite, thus leading to overall larger crystals.

We also examined the effect of the dispersed phase containing the NCs. We tested four solvents commonly used to disperse these NCs: chloroform, cyclohexane, hexane, and pentane (Figure 3b,c–f). The use of pentane as the dispersed phase results in largely amorphous superstructures, where the first reflection of the FCC crystallites can barely be distinguished from the broad features of the amorphous structure factor. Switching to hexane results in more prominent and brighter diffraction peaks, a trend that continues with cyclohexane and chloroform. The results, shown in Table 2, indicate that higher boiling points generally yield better crystals; we associate this with the lower evaporation rate of higher-boiling point solvents at a given temperature. Specifically, cyclohexane performs best, resulting in superstructures with a crystallinity of $X \approx 85\%$ and crystal sizes of $\xi \approx 300$ nm. However, chloroform, a solvent with a boiling point lower than cyclohexane, yields supercrystals of comparable quality to cyclohexane. We attribute this to the lower interfacial tension between chloroform and water (see Table 2), allowing the growth of higher-quality crystals similarly to what we observed previously by increasing surfactant concentration. Furthermore, while these superstructures are known to feature a minority hexagonal close-packed (HCP) phase,[16] using chloroform seems to suppress this behavior: The disappearance of the shoulder on the q_1 reflection,

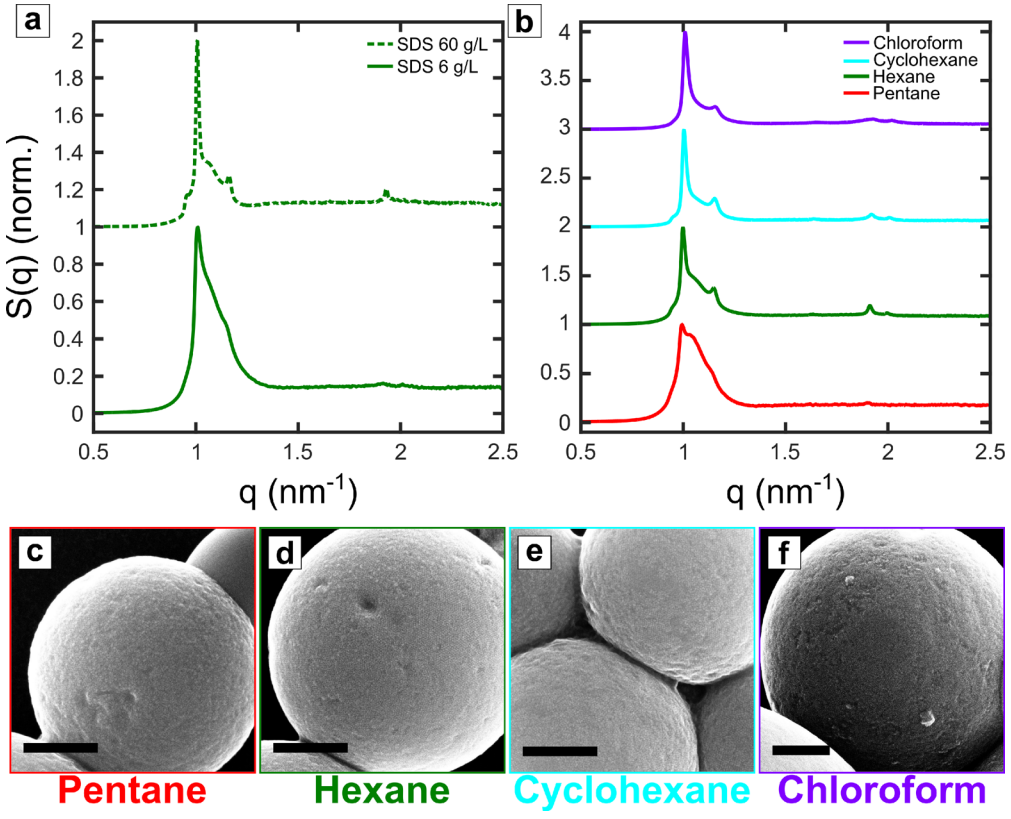

Figure 3. Influence of interfacial tension and solvent boiling point on supercrystal quality. (a) Structure factors of supercrystals consisting of σ = 5.6 ± 0.7 nm CdSe NCs, assembled at T = 40°C from a hexane emulsion in water with the indicated concentration of SDS. (b) Structure factors of supercrystals consisting of σ = 5.6 ± 0.7 nm CdSe NCs assembled at T = 20°C from a emulsion of the indicated hydrophobic solvent in 6 g/L SDS in water. (c–f) Secondary electron SEM micrographs corresponding to the samples measured in part b. Scale bars indicate 200 nm.

https://dx.doi.org/10.1021/acs.jpcc.0c02805
J. Phys. Chem. C 2020, 124, 11256–11264

Table 2. Influence of the Hydrophobic Solvent on the Final Quality of the Supercrystals Based on σ = 5.6 ± 0.7 nm CdSe NCs[a]

Solvent	Interfacial tension,[30b] mN/m	Solubility in water[30] mol %	Boiling point °C	Crystallinity, X %	Volume fraction, ϕ %	Crystal size, ξ nm
Pentane	49.0	1.01×10^{-3}	36	55.6 ± 0.1	27.6 ± 0.2	187.6 ± 0.4
Hexane	51.1	2.91×10^{-4}	68	73.8 ± 0.1	28.3 ± 0.2	291.1 ± 0.6
Cyclohexane	50.0	1.20×10^{-3}	81	83.9 ± 0.2	28.8 ± 0.2	298.8 ± 0.6
Chloroform	32.8	1.23×10^{-1}	61	81.7 ± 0.2	29.2 ± 0.2	286.1 ± 0.6

[a]Continuous phase: 6 g/L SDS in water; evaporation temperature: 20°C. [b]Reported interfacial tension values were measured in the absence of surfactant.

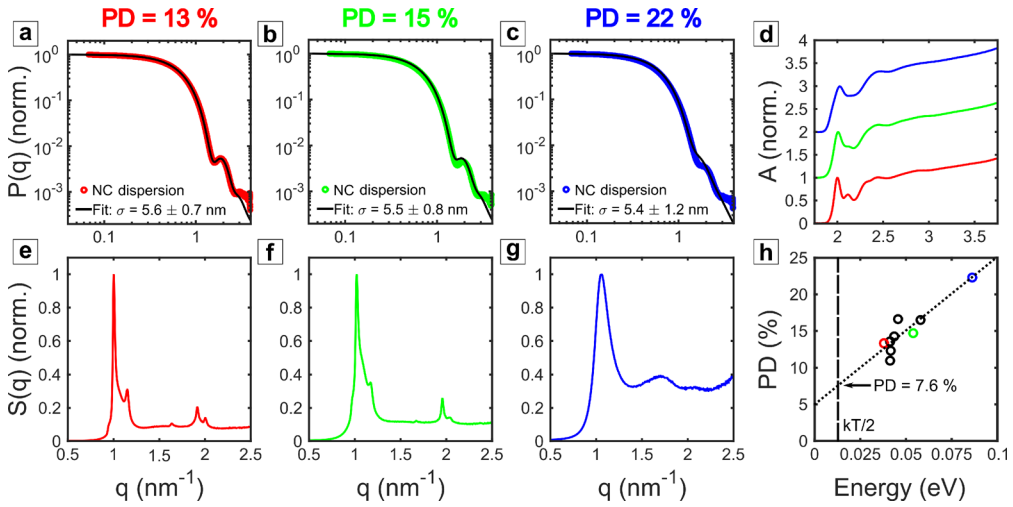

Figure 4. Influence of NC polydispersity on the final quality of supercrystals based on CdSe NCs. (Parts a–c) Determination of NC polydispersities from measured form factors.[24] Experimental form factors (dots) and fits to spherical form factors (solid lines) of NCs of comparable mean diameters and increasing polydispersity: (a) σ = 5.6 ± 0.7 nm, (b) σ = 5.5 ± 0.8 nm, (c) σ = 5.4 ± 1.2 nm. (d) Absorption spectra measured from dispersions of NCs described in parts a–c. (e–g) Structure factors measured from supercrystals consisting of NCs described in parts a–c, respectively, dried at 20 °C from a cyclohexane emulsion stabilized by 6 g/L SDS in water. (h) Dependence of the NC polydispersity, determined through SAXS, on the half-width at half-maximum (HWHM) of the lowest-energy excitonic transition, determined through spectrophotometry. Colored dots correspond to the samples described in parts a–g. The dotted line indicates the linear fit: PD (%) = 5.015 + 201.2 × HWHM (eV).

previously identified as the 100 HCP reflection,[16] as well as the enhanced dip of the signal between q_1 and q_2, seems to suggest that the HCP phase does no longer nucleate. Since, in the case of hard spheres, the HCP phase is expected to preferentially nucleate at the interface between oil and water,[17] we suggest that the formation of this secondary phase is energetically discouraged by the more flexible interface due to the lower surface tension of the system.

NC Polydispersity. Classic experimental[31] and theoretical[19] studies how that crystal nucleation becomes increasingly suppressed in colloidal dispersions of hard spheres when the polydispersity increases above 9%, where the polydispersity is defined as the ratio between the standard deviation and the average radius of a distribution of spheres. A more recent study has shown that hard spheres of polydispersity up to 19% can still crystallize if compressed slowly enough, favoring the formation of binary phases.[32] Therefore, we investigate the crystallization behavior of NCs of increasing polydispersity, while maintaining all other assembly parameters constant, as shown in Figure 4. As determined from the form factors measured by X-ray scattering, the polydispersities for the NC core of the three samples are 13, 15, and 22%; see Figure 4a–c. We also used the width of the first exciton peak as an independent measure of the polydispersity and find a closely linear relation (correlation coefficient r = 0.92) with the polydispersities determined from the form factor (Figure 4d,h) validating this polydispersity measurement. At room temperature, we expect this spectroscopic measurement for polydispersity to become insensitive to polydispersities below 7.6 for CdSe, when the width of the electronic transition is expected to saturate to $kT \approx 0.026$ eV.

Remarkably, NCs with a 13% polydisperse core still crystallize into superstructures, as shown in Figure 4e. Nevertheless, as the polydispersity increases from 13 to 15%, the crystalline reflections begin to broaden, suggesting a decrease in average crystal size from $\xi \approx 284$ nm to 260 nm; see Figure 4f. At a polydispersity of 22%, the structure factor of assembled NCs does not show any sharp reflections, only broad features consistent with the formation of an amorphous structure, Figure 4g. This simple experiment clearly illustrates the presence of a polydispersity threshold for the NC core, between 15 and 22%, beyond which crystal formation becomes suppressed. We conclude that crystallization in NCs is favored when compared to hard spheres. The higher polydispersity threshold may be mediated by the soft ligand shell, which efficiently fills the empty spaces between NCs of dissimilar sizes.[33,34] Furthermore, while SAXS measurements may not be readily available to most laboratories, we demonstrate that the polydispersity extracted from SAXS scales linearly with the half-width at half-maximum (HWHM) of the first exciton

https://dx.doi.org/10.1021/acs.jpcc.0c02805
J. Phys. Chem. C 2020, 124, 11256–11264

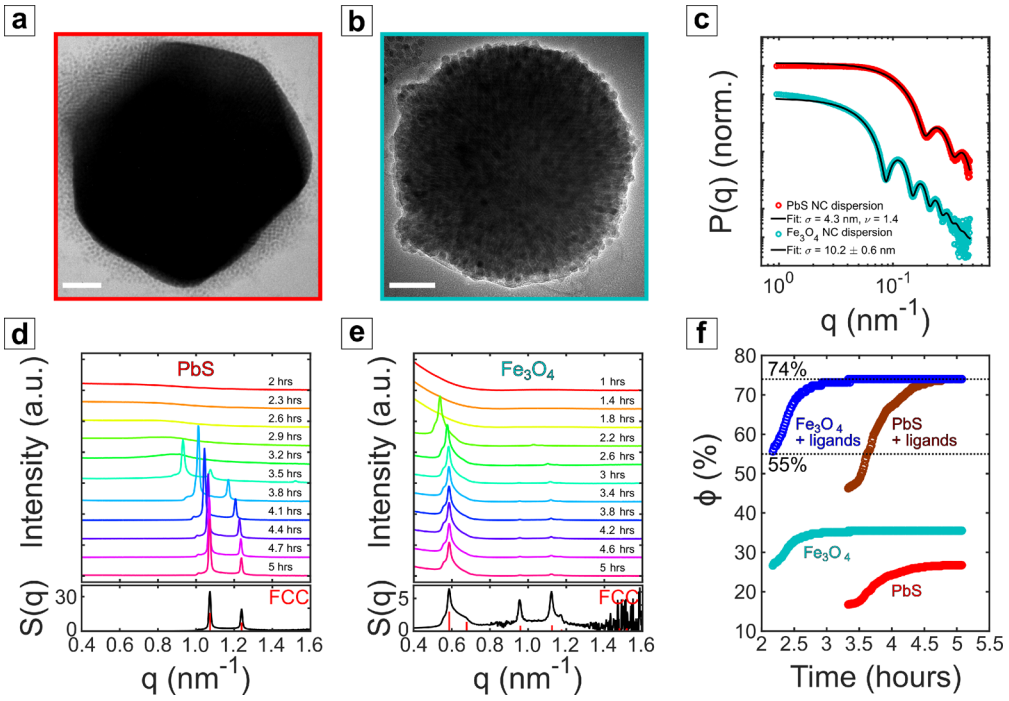

Figure 5. In situ observation of supercrystal formation. Transmission electron micrographs of supercrystals of (a) PbS and (b) Fe_3O_4 NCs. Scale bars indicate 50 nm. (c) Experimental form factors (symbols) and fit (solid lines) of PbS and Fe_3O_4 NCs. Azimuthally averaged SAXS patterns of (d) PbS and (e) Fe_3O_4 NCs undergoing crystallization while dispersed within toluene droplets in 24 g/L SDS in water at 70°C. Time stamps are indicated for each curve. The structure factor, $S(q)$, extracted from the last curve is shown at the bottom of each panel. Expected positions for FCC reflections are indicated by red ticks. (f) Kinetic evolution of the FCC volume fraction, ϕ, relative to the inorganic core of NCs (lighter symbols) as well as to their hard sphere size (darker symbols). The dotted lines indicated the hard sphere melting transition, $\phi \approx 55\%$, and close packing, $\phi \approx 74\%$.

peak, experimentally justifying the use of sharpness of absorption features to gauge particle polydispersity, Figure 4d,h.[35]

Crystallization of PbS and Fe_3O_4 NCs into FCC Supercrystals. We illustrate the generality of the emulsion template by extending the assembly process to technologically relevant PbS and Fe_3O_4 NCs. PbS semiconductor NCs are promising candidates as nanoscale building blocks for next-generation optoelectronic devices, such as solar cells and photodetectors, since their bandgap can be tuned across the near-infrared to the optimal range for photovoltaics, 1.1−1.4 eV, and telecommunications, 0.8 eV.[36,37] Several studies have recently focused on the evaporation of a NC dispersion on a substrate, highlighting that these NCs can crystallize in a number of structures such as FCC, HCP, body-centered cubic (BCC), and body-centered tetragonal (BCT) thus posing a severe limit to the reproducibility of these superstructures.[38−41] This poses a major motivation to investigate the assembly of PbS NCs using the emulsion template, where an improved structural reproducibility may be expected as a consequence of the slow and well-controlled solvent evaporation rate. Fe_3O_4 NCs are interesting as they exhibit superparamagnetism: The NCs display null magnetization when no external field is applied and coherently magnetize upon the application of an external magnetic field.[42] The magnetic properties of these NCs can be tuned by changing their size, shape, and composition and feature a wide range of applications in magnetic shielding, magnetic separation, medical diagnostics, and clinical therapy.

We synthesize PbS and Fe_3O_4 NCs according to recently published methods.[22,43] Measuring their form factor reveals that the PbS NCs can be well-described as slightly prolate ellipsoids, with an equatorial diameter of $\sigma = 4.3$ nm and an aspect ratio of $\nu = 1.4$, while the Fe_3O_4 are better described as spheres with a diameter of $\sigma = 10.2 \pm 0.6$ nm, Figure 5c. Assembling these NCs by using a toluene-in-water template yields superstructures similar in size but featuring significantly distinct morphologies. The PbS NCs crystallize into supercrystals with well-defined facets, while the Fe_3O_4 supercrystals assume a more isotropic morphology, as shown in Figure 5a,b, respectively.

We investigate the crystallization kinetics of these two distinct NC systems under identical assembly conditions of temperature, initial volume fraction, and surfactant concentration by monitoring the SAXS pattern during droplet evaporation using a recently developed method.[16] At early times, the azimuthally averaged scattering pattern features a diffuse signal corresponding to a dilute dispersion of PbS NCs dispersed within the emulsion droplets, as shown in Figure 5d. After 3.2 h of drying, a broad feature begins to emerge from the background around 0.8 nm^{-1}. Within a few minutes, this broad signal develops into three distinct reflection peaks. Over the course of additional 1.5 h, these peaks shift toward larger wavevectors while increasing in intensity and sharpness. These real-time observations describe the process of nucleation, followed by the simultaneous growth and compression of the supercrystalline lattice.[16] By dividing the late-time scattering pattern by the form factor, we can extract the structure factor shown at the bottom of Figure 5d, consistent with a FCC structure of average crystal size $\xi \approx 592$ nm and a surface-to-surface distance between nearest neighbors of $d \approx 2.0$ nm, as

https://dx.doi.org/10.1021/acs.jpcc.0c02805
J. Phys. Chem. C 2020, 124, 11256−11264

calculated by the difference between the nearest-neighbor distance and the average NC diameter.

Despite the difference in NC size and morphology, the crystallization of Fe_3O_4 NCs follows a similar pathway as PbS NCs, as shown in Figure 5e. Following supercrystal nucleation after 2 h of drying, five reflection peaks emerge from the diffuse background signal and shift toward higher q as a function of time, as a result of supercrystal compression. Similarly to the case of PbS NCs, the superstructure is FCC, with an average crystal size of $\xi \approx 277$ nm and $d \approx 2.9$ nm.

We quantitatively compare the crystallization kinetics of PbS and Fe_3O_4 NCs by tracking the inorganic volume fraction ϕ of the NCs as a function of time in Figure 5f. Here, we notice that supercrystal nucleation takes place at significantly different volume fractions for the two samples: $\phi_c \approx 16.7\%$ for PbS NCs and 26.7% for Fe_3O_4. After nucleation, the volume fraction increases as a function of time to plateau at 26.7 and 35.6% for PbS and Fe_3O_4, respectively. If we assume the presence of a uniform ligand shell of thickness l surrounding the inorganic NC core of diameter σ, we can attribute the difference in volume fraction between the two samples to the fact that the volume ratio of the organic ligand shell to the inorganic NC core decreases according to

$$[(\sigma/2 + l)^3 - (\sigma/2)^3]/(\sigma/2)^3 = (1 + 2l/\sigma)^3 - 1$$

as σ increases. We note that the CdSe NCs used in this paper have an intermediate diameter between the PbS and Fe_3O_4 NCs and accordingly crystallize with an average final volume fraction of 28.6%, which is intermediate between PbS and Fe_3O_4. The increasing relevance of the ligand shell to the crystallization of smaller NCs is also likely responsible for the delayed nucleation of the PbS sample which takes place more than 1 h later than the Fe_3O_4 despite beginning the experiment with the same inorganic volume fraction, $\phi = 0.1\%$.

To quantitatively compare the crystallization behavior of NCs to the well-established case of hard spheres, we define an effective NC diameter, $\sigma_{eff} = \sigma + d$, thus accounting for the ligand shell.[16] By doing so, we can track the effective volume fraction of the NCs, including the contribution of the ligands, as a function of time. This treatment shows that crystal nucleation takes place between 45% and 55% volume fraction, corresponding to the melting transition of hard spheres, and eventually plateaus at ≈74%, corresponding to close packing in FCC structures.

CONCLUSIONS

The growth of high-quality supercrystals based on NCs is of great interest to the development of reliable novel optoelectronic devices based on NCs. We have shown that emulsion-templated assembly has the potential to satisfy these needs by providing the means to assemble supercrystals in a reproducible fashion and close to single-crystal quality. We have investigated the influence of different axes of the parameter space that governs this type of assembly and the combinations that yield the largest crystals with grain sizes up to 600 nm. Specifically, slower drying induces the growth of the largest crystalline domains, while faster drying, at temperatures comparable to the boiling point of the dispersed phase of the emulsion, yields amorphous structures, Figure 2. Additionally, a decrease in the interfacial tension between dispersed and continuous phases is beneficial to the growth of supercrystals with larger grain sizes. This can be achieved either by (1) increasing the surfactant concentration and/or by (2) changing the solvent composing the dispersed phase, Figure 3. Furthermore, NC polydispersity can suppress the formation of supercrystals. Larger supercrystal grain sizes correlate with the most monodisperse NCs, with a crystallization threshold between 15% and 22% polydispersity, Figure 4.

We are confident that the generality of these results will contribute to shape the growing field of superparticle assembly[13] and its implications on photonics,[44] electronics, magnetics,[45] and catalysis.

ASSOCIATED CONTENT

Supporting Information

The Supporting Information is available free of charge at https://pubs.acs.org/doi/10.1021/acs.jpcc.0c02805.

Detailed description of NC synthesis, emulsion-templated assembly, and characterization techniques (PDF)

AUTHOR INFORMATION

Corresponding Author

Peter Schall − *Van der Waals - Zeeman Institute, University of Amsterdam, 1098XH Amsterdam, The Netherlands;* Email: p.schall@uva.nl

Authors

Emanuele Marino − *Van der Waals - Zeeman Institute, University of Amsterdam, 1098XH Amsterdam, The Netherlands; Department of Chemistry, University of Pennsylvania, Philadelphia, Pennsylvania 19104, United States;* orcid.org/0000-0002-0793-9796

Austin W. Keller − *Department of Materials Science and Engineering, University of Pennsylvania, Philadelphia, Pennsylvania 19104, United States*

Di An − *Department of Chemistry, University of Pennsylvania, Philadelphia, Pennsylvania 19104, United States*

Sjoerd van Dongen − *Physical Chemistry and Soft Matter, Wageningen University and Research, 6708WE Wageningen, The Netherlands; Department of Chemistry, University of Pennsylvania, Philadelphia, Pennsylvania 19104, United States*

Thomas E. Kodger − *Physical Chemistry and Soft Matter, Wageningen University and Research, 6708WE Wageningen, The Netherlands*

Katherine E. MacArthur − *Ernst Ruska Centre for Microscopy and Spectroscopy with Electrons and Peter Grünberg Institute, Forschungszentrum Jülich GmbH, 52425 Jülich, Germany;* orcid.org/0000-0002-5024-2054

Marc Heggen − *Ernst Ruska Centre for Microscopy and Spectroscopy with Electrons and Peter Grünberg Institute, Forschungszentrum Jülich GmbH, 52425 Jülich, Germany*

Cherie R. Kagan − *Department of Electrical and Systems Engineering, Department of Materials Science and Engineering, and Department of Chemistry, University of Pennsylvania, Philadelphia, Pennsylvania 19104, United States;* orcid.org/0000-0001-6540-2009

Christopher B. Murray − *Department of Chemistry and Department of Materials Science and Engineering, University of Pennsylvania, Philadelphia, Pennsylvania 19104, United States*

Complete contact information is available at: https://pubs.acs.org/10.1021/acs.jpcc.0c02805

https://dx.doi.org/10.1021/acs.jpcc.0c02805
J. Phys. Chem. C 2020, 124, 11256−11264

Notes

The authors declare no competing financial interest.

■ ACKNOWLEDGMENTS

This work is part of the research program "Nanoarchitectures: Smart Assembly, Quantum Electronics and Soft Mechanics" with project number 680.47.615, which is financed by the Dutch Research Council (NWO). P.S. and T.E.K. acknowledge financial support from NWO through personal Vici and Veni grants, respectively. Beamtime at BM26B "DUBBEL" beamline, ESRF was supported through NWO funding, experiment no. 26-02-841. E.M., C.R.K., and C.B.M. acknowledge primary support from the Office of Naval Research Multidisciplinary University Research Initiative Award ONR N00014-18-1-2497. A.W.K. and C.R.K. acknowledge support from the Semiconductor Research Corporation (SRC) under the Nanomanufacturing Materials and Processes (NMP) trust via Task 2797.001. C.B.M. acknowledges the Richard Perry University Professorship at the University of Pennsylvania. Support for the Dual Source and Environmental X-ray Scattering Facility at the University of Pennsylvania was provided by the Laboratory for Research on the Structure of Matter which is funded in part by NSF MRSEC 1720530. This research used resources of the Center for Functional Nanomaterials and the National Synchrotron Light Source II, which are U.S. DOE Office of Science Facilities, at Brookhaven National Laboratory under Contract No. DE-SC0012704. The authors thank D.H. Merino, E.H.R. Tsai, A. Capretti, S. Yang, and D. Rosen for assistance with X-ray data collection.

■ REFERENCES

(1) Boles, M. A.; Engel, M.; Talapin, D. V. Self-Assembly of Colloidal Nanocrystals: From Intricate Structures to Functional Materials. *Chem. Rev.* **2016**, *116*, 11220−11289.
(2) Bishop, K. J. M.; Wilmer, C. E.; Soh, S.; Grzybowski, B. A. Nanoscale Forces and Their Uses in Self-Assembly. *Small* **2009**, *5*, 1600−1630.
(3) Marino, E.; Balazs, D. M.; Crisp, R. W.; Hermida-Merino, D.; Loi, M. A.; Kodger, T. E.; Schall, P. Controlling Superstructure−Property Relationships via Critical Casimir Assembly of Quantum Dots. *J. Phys. Chem. C* **2019**, *123*, 13451−13457.
(4) Hanrath, T. Colloidal nanocrystal quantum dot assemblies as artificial solids. *J. Vac. Sci. Technol., A* **2012**, *30*, 030802.
(5) Choi, J.-H.; Fafarman, A. T.; Oh, S. J.; Ko, D.-K.; Kim, D. K.; Diroll, B. T.; Muramoto, S.; Gillen, J. G.; Murray, C. B.; Kagan, C. R. Bandlike transport in strongly coupled and doped quantum dot solids: a route to high-performance thin-film electronics. *Nano Lett.* **2012**, *12*, 2631−2638.
(6) Crisp, R. W.; Schrauben, J. N.; Beard, M. C.; Luther, J. M.; Johnson, J. C. Coherent Exciton Delocalization in Strongly Coupled Quantum Dot Arrays. *Nano Lett.* **2013**, *13*, 4862−4869.
(7) Kagan, C. R.; Murray, C. B. Charge transport in strongly coupled quantum dot solids. *Nat. Nanotechnol.* **2015**, *10*, 1013.
(8) Lan, X.; Chen, M.; Hudson, M. H.; Kamysbayev, V.; Wang, Y.; Guyot-Sionnest, P.; Talapin, D. V. Quantum dot solids showing state-resolved band-like transport. *Nat. Mater.* **2020**.
(9) Lacava, J.; Born, P.; Kraus, T. Nanoparticle Clusters with Lennard-Jones Geometries. *Nano Lett.* **2012**, *12*, 3279−3282.
(10) de Nijs, B.; Dussi, S.; Smallenburg, F.; Meeldijk, J. D.; Groenendijk, D. J.; Filion, L.; Imhof, A.; van Blaaderen, A.; Dijkstra, M. Entropy-driven formation of large icosahedral colloidal clusters by spherical confinement. *Nat. Mater.* **2015**, *14*, 56.
(11) Kister, T.; Mravlak, M.; Schilling, T.; Kraus, T. Pressure-controlled formation of crystalline, Janus, and core−shell supraparticles. *Nanoscale* **2016**, *8*, 13377−13384.
(12) Wang, P.-p.; Qiao, Q.; Zhu, Y.; Ouyang, M. Colloidal Binary Supracrystals with Tunable Structural Lattices. *J. Am. Chem. Soc.* **2018**, *140*, 9095−9098.
(13) Wintzheimer, S.; Granath, T.; Oppmann, M.; Kister, T.; Thai, T.; Kraus, T.; Vogel, N.; Mandel, K. Supraparticles: Functionality from Uniform Structural Motifs. *ACS Nano* **2018**, *12*, 5093−5120.
(14) Miyazaki, H.; Inasawa, S. Drying kinetics of water droplets stabilized by surfactant molecules or solid particles in a thin non-volatile oil layer. *Soft Matter* **2017**, *13*, 8990−8998.
(15) Auer, S.; Frenkel, D. Prediction of absolute crystal-nucleation rate in hard-sphere colloids. *Nature* **2001**, *409*, 1020−1023.
(16) Marino, E.; Kodger, T. E.; Wegdam, G. H.; Schall, P. Revealing Driving Forces in Quantum Dot Supercrystal Assembly. *Adv. Mater.* **2018**, *30*, 1803433.
(17) Montanarella, F.; Geuchies, J. J.; Dasgupta, T.; Prins, P. T.; van Overbeek, C.; Dattani, R.; Baesjou, P.; Dijkstra, M.; Petukhov, A. V.; van Blaaderen, A.; et al. Crystallization of Nanocrystals in Spherical Confinement Probed by in Situ X-ray Scattering. *Nano Lett.* **2018**, *18*, 3675−3681.
(18) Boles, M. A.; Talapin, D. V. Many-Body Effects in Nanocrystal Superlattices: Departure from Sphere Packing Explains Stability of Binary Phases. *J. Am. Chem. Soc.* **2015**, *137*, 4494−4502.
(19) Auer, S.; Frenkel, D. Suppression of crystal nucleation in polydisperse colloids due to increase of the surface free energy. *Nature* **2001**, *413*, 711.
(20) Chernomordik, B. D.; Marshall, A. R.; Pach, G. F.; Luther, J. M.; Beard, M. C. Quantum Dot Solar Cell Fabrication Protocols. *Chem. Mater.* **2017**, *29*, 189−198.
(21) Weidman, M. C.; Beck, M. E.; Hoffman, R. S.; Prins, F.; Tisdale, W. A. Monodisperse, Air-Stable PbS Nanocrystals via Precursor Stoichiometry Control. *ACS Nano* **2014**, *8*, 6363−6371.
(22) Park, J.; An, K.; Hwang, Y.; Park, J.-G.; Noh, H.-J.; Kim, J.-Y.; Park, J.-H.; Hwang, N.-M.; Hyeon, T. Ultra-large-scale syntheses of monodisperse nanocrystals. *Nat. Mater.* **2004**, *3*, 891−895.
(23) Yu, W. W.; Qu, L.; Guo, W.; Peng, X. Experimental Determination of the Extinction Coefficient of CdTe, CdSe, and CdS Nanocrystals. *Chem. Mater.* **2003**, *15*, 2854−2860.
(24) Murray, C. B.; Kagan, C. R.; Bawendi, M. G. Synthesis and Characterization of Monodisperse Nanocrystals and Close-Packed Nanocrystal Assemblies. *Annu. Rev. Mater. Sci.* **2000**, *30*, 545−610.
(25) Cho, K.-S.; Talapin, D. V.; Gaschler, W.; Murray, C. B. Designing PbSe Nanowires and Nanorings through Oriented Attachment of Nanoparticles. *J. Am. Chem. Soc.* **2005**, *127*, 7140−7147.
(26) Weeks, E. R.; Crocker, J. C.; Levitt, A. C.; Schofield, A.; Weitz, D. A. Three-Dimensional Direct Imaging of Structural Relaxation Near the Colloidal Glass Transition. *Science* **2000**, *287*, 627.
(27) Harland, J. L.; van Megen, W. Crystallization kinetics of suspensions of hard colloidal spheres. *Phys. Rev. E: Stat. Phys., Plasmas, Fluids, Relat. Interdiscip. Top.* **1997**, *55*, 3054−3067.
(28) Schöpe, H. J.; Bryant, G.; van Megen, W. Effect of polydispersity on the crystallization kinetics of suspensions of colloidal hard spheres when approaching the glass transition. *J. Chem. Phys.* **2007**, *127*, 084505.
(29) Patterson, A. L. The Scherrer Formula for X-Ray Particle Size Determination. *Phys. Rev.* **1939**, *56*, 978−982.
(30) Demond, A. H.; Lindner, A. S. Estimation of interfacial tension between organic liquids and water. *Environ. Sci. Technol.* **1993**, *27*, 2318−2331.
(31) Pusey, P. N. The effect of polydispersity on the crystallization of hard spherical colloids. *J. Phys.* **1987**, *48*, 709−712.
(32) Bommineni, P. K.; Varela-Rosales, N. R.; Klement, M.; Engel, M. Complex Crystals from Size-Disperse Spheres. *Phys. Rev. Lett.* **2019**, *122*, 128005.
(33) Alsayed, A. M.; Islam, M. F.; Zhang, J.; Collings, P. J.; Yodh, A. G. Premelting at Defects Within Bulk Colloidal Crystals. *Science* **2005**, *309*, 1207.
(34) Jishkariani, D.; Elbert, K. C.; Wu, Y.; Lee, J. D.; Hermes, M.; Wang, D.; van Blaaderen, A.; Murray, C. B. Nanocrystal Core Size and

https://dx.doi.org/10.1021/acs.jpcc.0c02805
J. Phys. Chem. C 2020, 124, 11256−11264

Shape Substitutional Doping and Underlying Crystalline Order in Nanocrystal Superlattices. *ACS Nano* **2019**, *13*, 5712−5719.
(35) Murray, C. B.; Norris, D. J.; Bawendi, M. G. Synthesis and characterization of nearly monodisperse CdE (E= sulfur, selenium, tellurium) semiconductor nanocrystallites. *J. Am. Chem. Soc.* **1993**, *115*, 8706−8715.
(36) Sargent, E. H. Colloidal quantum dot solar cells. *Nat. Photonics* **2012**, *6*, 133.
(37) Saran, R.; Curry, R. J. Lead sulphide nanocrystal photodetector technologies. *Nat. Photonics* **2016**, *10*, 81.
(38) Bian, K.; Choi, J. J.; Kaushik, A.; Clancy, P.; Smilgies, D.-M.; Hanrath, T. Shape-Anisotropy Driven Symmetry Transformations in Nanocrystal Superlattice Polymorphs. *ACS Nano* **2011**, *5*, 2815−2823.
(39) Weidman, M. C.; Smilgies, D.-M.; Tisdale, W. A. Kinetics of the self-assembly of nanocrystal superlattices measured by real-time in situ X-rayÂ scattering. *Nat. Mater.* **2016**, *15*, 775−781.
(40) Lokteva, I.; Koof, M.; Walther, M.; Grübel, G.; Lehmkühler, F. Monitoring Nanocrystal Self-Assembly in Real Time Using In Situ Small-Angle X-Ray Scattering. *Small* **2019**, *15*, 1900438.
(41) Lokteva, I.; Koof, M.; Walther, M.; Grübel, G.; Lehmkühler, F. Coexistence of hcp and bct Phases during In Situ Superlattice Assembly from Faceted Colloidal Nanocrystals. *J. Phys. Chem. Lett.* **2019**, *10*, 6331−6338.
(42) Faraudo, J.; Andreu, J. S.; Camacho, J. Understanding diluted dispersions of superparamagnetic particles under strong magnetic fields: a review of concepts, theory and simulations. *Soft Matter* **2013**, *9*, 6654−6664.
(43) Voznyy, O.; Levina, L.; Fan, J. Z.; Askerka, M.; Jain, A.; Choi, M.-J.; Ouellette, O.; Todorović, P.; Sagar, L. K.; Sargent, E. H. Machine Learning Accelerates Discovery of Optimal Colloidal Quantum Dot Synthesis. *ACS Nano* **2019**, *13*, 11122−11128.
(44) Montanarella, F.; Urbonas, D.; Chadwick, L.; Moerman, P. G.; Baesjou, P. J.; Mahrt, R. F.; van Blaaderen, A.; Stöferle, T.; Vanmaekelbergh, D. Lasing Supraparticles Self-Assembled from Nanocrystals. *ACS Nano* **2018**, *12*, 12788−12794.
(45) Yang, Y.; Wang, B.; Shen, X.; Yao, L.; Wang, L.; Chen, X.; Xie, S.; Li, T.; Hu, J.; Yang, D.; et al. Scalable Assembly of Crystalline Binary Nanocrystal Superparticles and Their Enhanced Magnetic and Electrochemical Properties. *J. Am. Chem. Soc.* **2018**, *140*, 15038−15047.

https://dx.doi.org/10.1021/acs.jpcc.0c02805
J. Phys. Chem. C 2020, 124, 11256−11264